Skin Pharmacology and Physiology

Research Article

Skin Pharmacol Physiol
DOI: 10.1159/000547514

Received: March 26, 2025
Accepted: July 9, 2025
Published online: October 16, 2025

Impact of Scattering Variation Measured by Line-Field Confocal Optical Coherence Tomography on Fluorescence Measurement by Optical Spectroscopy: A Study on Phantoms and Human Skin Models

Sergey M. Zaytsev[a] Walter Blondel[a] Jonas Ogien[b] Arnaud Dubois[b, c] Marine Amouroux[a]

[a]Université de Lorraine, CNRS, CRAN, Nancy, France; [b]DAMAE Medical, Paris, France; [c]Laboratoire Charles Fabry, Université Paris-Saclay, Institut d'Optique Graduate School, CNRS, Palaiseau, France

Keywords
Line-filed confocal optical coherence tomography · Fluorescence spectroscopy · Human skin model · Optical phantoms · Optical properties · Scattering

Abstract
Introduction: Since skin tissues feature highly inter- and intraindividual variable scattering properties, it is of interest for fluorescence spectroscopy applied to skin cancer diagnostic assistance to be combined with a device able to measure scattering properties of skin tissues in vivo and further correct fluorescence spectra. This study aimed to explore the interest of combining two devices previously used in vivo during clinical trials: line-field confocal optical coherence tomography (LC-OCT) for scattering property estimation and fluorescence spectroscopy for measuring the modification of endogenous fluorescence induced by carcinogenesis. ***Methods:*** This study was performed on liquid phantoms and on commercially available in vitro-grown 3D human skin models. Bulk scattering properties of liquid fluorescent phantoms were estimated separately at 800 nm as a function of intralipid concentration from LC-OCT images using a model based on the modified Beer-Lambert law. These results were then compared with values obtained with double-integrating spheres and collimated transmittance measurements followed by inverse adding-doubling estimation of bulk scattering properties. Changes in the amplitude of the chlorin-e6 fluorescence peak were measured as a function of IL concentration using fluorescence spectroscopy. The results obtained on phantoms were then validated with the in vitro-grown skin model. ***Results:*** Measurements performed on liquid phantoms showed that LC-OCT overestimates scattering coefficient and anisotropy factor by approximately 20–30% compared to values measured by a method (useable only ex vivo) considered here as the gold standard: double-integrating spheres-based optical bench. Fluorescence spectroscopy was employed to measure changes in chlorin-e6 fluorescence-measured intensity relative to varying intralipid concentration. Optical characterization of human skin models confirmed their similarity with in vivo human skin in terms of morphology and of autofluorescence signals. LC-OCT was used to detect dermal scattering coefficient increase induced by impregnating the artificial skin with a PEG-400/DMSO

karger@karger.com
www.karger.com/spp

Correspondence to:
Marine Amouroux, marine.amouroux@univ-lorraine.fr

solution that usually acts as an optical clearing agent. However, the observed effect was opposite to the typically expected decrease in the scattering coefficient, which was likely attributable to specific morphological features of the artificial skin that hindered the clearing process, resulting in only hyperosmotic effect. Spectral measurements supported these findings. ***Conclusion:*** These findings underscore the interest of combining both optical methods, LC-OCT imaging and autofluorescence spectroscopy, to assess pathology-related fluorophore and scattering alterations in vivo.

Introduction

Optical methods, which rely on the interaction of light with biological tissues, have shown significant diagnostic potential as a supplement or alternative to histology, the gold standard method [1]. These methods are valued for their noninvasiveness, high sensitivity, ability to provide real-time information without the need for time-consuming histological sample preparation, and their potential for in vivo clinical application [2]. Some techniques provide morphological information, while others give access to functional information. Combining both types of information allows a more complete understanding of pathological processes [3].

Imaging methods are able to provide morphological information about skin structure modifications. Line-field confocal optical coherence tomography (LC-OCT) is an advanced optical imaging technique that merges the strengths of both optical coherence tomography (OCT) and confocal microscopy. It enables the acquisition of three-dimensional (3D) tissue images with an isotropic resolution of approximately 1 μm, sufficient to visualize cells (their nucleus) within epidermis [4]. Numerous studies have highlighted the effectiveness of LC-OCT in providing real-time in vivo assistance to skin cancer diagnosis [5–9]. In addition to optical imaging, various spectral methods, such as fluorescence, diffuse reflectance (DR), and Raman spectroscopy, can provide functional (e.g., metabolic) information about the tissue, revealing pathology-induced chemical modifications. This has prompted recent interest in combining imaging techniques with spectral methods to obtain both morphological and functional data [3, 10–13].

Light propagation through skin is governed by the wavelength-dependent bulk optical properties of the tissue, including the bulk absorption coefficient (μ_a), bulk scattering coefficient (μ_s), and anisotropy factor (g) [14], which are determined by the size, shape, and density of tissue constituents. In both imaging and spectroscopy approaches, knowledge about the bulk optical properties enables the correct understanding and interpretation of the measured optical signals. For example, it allows to estimate the concentration (or volume fraction) of scatterers and fluorophores within the sample [15, 16].

One technical solution for measuring the optical properties of ex vivo biological samples is the use of a "double-integrating sphere" (DIS) optical bench including a tunable supercontinuum laser and two integrating spheres to measure total transmittance and DR spectra [17]. Collimated transmittance is measured using a third photodetector located "far" (about 1 m away) from the sample. After performing the three types of measurements, the resulting values serve as input data for the so-called inverse adding-doubling (IAD) algorithm available online [18]. Output data provided by the IAD program are spectral values of anisotropy, absorption, and scattering coefficients (g, μ_a, μ_s). Such an approach implies ex vivo use only, which is unsuitable for in vivo clinical measurements on patients.

The first noninvasive in vivo techniques for determining the optical properties of biological tissues were based on optical imaging methods, such as OCT. They usually allow to estimate attenuation coefficient μ_t which is the sum of scattering and absorption coefficient [19–21].

It is also necessary to evaluate the optical properties μ_s and g separately. This is because each of them provides a different information on the structure of the biological tissue under study and allows for more comprehensive information to be obtained on pathological processes in the tissue. Jacques [22] developed a method based on reflectance confocal microscopy images, which enables the μ_s and g optical properties to be assessed separately, in an approach quite similar to that based on optical bench and the IAD algorithm, but this time offering the possibility of assessing these properties noninvasively on in vivo samples. Our team has recently applied this technique to the characterization and evaluation of optical property modifications induced by optical clearing (OC) on optical phantoms and on human skin in vivo [23, 24]. The method proposed by Steven Jacques (based on image intensity profile fitting and a modified Beer-Lambert law) is preferred to the other methods developed, because it applies to a wider range of situations and is more robust to particular cases of optical properties [25, 26].

Considering the problems mentioned, the main objective of this work was to validate the possibility of

separately assessing the bulk optical properties μ_s and g of tissue-mimicking liquid phantoms as a function of the volume fraction of scattering particles using LC-OCT images, having the potential to be applied, unlike the DIS-optical bench, to in vivo tissues. The fluorescence spectrum of chlorin e6 (Ce6) as a part of the phantoms was also analyzed as a function of the concentration of scattering particles. The second objective of the study was to validate whether the observations made on liquid phantoms could be reproduced on more complex models, closer to human skin in terms of biochemical composition: in vitro skin models grown in 3D. In this latter case, autofluorescence (AF) was measured and scattering properties were made variable using OC. To our knowledge, the data presented in this paper are the first to demonstrate optical characterization of such human skin models in terms of AF and of scattering and anisotropy coefficient estimation. Moreover, thanks to data previously acquired on patients, data acquired on 3D models grown in vitro could be compared with data acquired on healthy skin in vivo.

Materials and Methods

Optical Techniques for Characterizing Phantoms and Human Skin Models

DIS Optical Bench and LC-OCT for Estimation of μ_s and g

The DIS-optical bench consists of a supercontinuum white-light fiber laser (SuperK Fianium FIU15, NKT Photonics®) providing a collimated laser beam (1-mm beam diameter, 5-nm full width at half maximum for each band, minimum 1-mW power/band) thanks to a computer-controlled variable bandwidth filter (SuperK VARIA, NKT Photonics®) that tunes the center wavelength from 405 to 840 nm. The IAD algorithm developed and optimized by Prahl [18] was used to estimate the scattering coefficient $\mu_s(\lambda)$ and anisotropy factor $g(\lambda)$ of liquid phantoms from the DR, total transmittance, and collimated transmittance spectra acquired on the DIS-optical bench.

For full details on the LC-OCT device (DeepLive™, DAMAE Medical, France) employed in this study, refer to reference [5]. In summary, this system is based on a Linnik interferometer design and utilizes line illumination from a supercontinuum laser with a center wavelength near 800 nm. Each interferometer arm includes a water-immersion microscope objective with a numerical aperture (NA) = 0.5. Using a line camera, the system detects the spatially coherent light backscattered by the tissue. By scanning along the z-axis during the acquisition of horizontal sectional images (covering a field of view of 1.2 mm × 0.5 mm along x- and y-axes), it assembles an image stack to render a 3D representation of the tissue in situ. The device achieves an axial and lateral resolution of 1.3 µm, with a maximum penetration depth (z) of around 500 µm. In LC-OCT, the focus is dynamically adjusted as a function of depth during the depth scan. This allows the use of high NA optics to achieve high lateral resolution. Unlike traditional OCT systems, a large depth of field is not required in LC-OCT. Additionally, there is no roll-off effect, as the technique is based on time-domain OCT.

A comprehensive explanation of the model introduced by Jacques et al. [22] and later adapted by Waszczuk et al. [23] to the LC-OCT imaging system can be found in their respective works [24]. In short, to estimate the bulk optical properties of scattering media, a modified exponential decay model of the depth-resolved reflectance $R(z)$, as proposed by Jacques et al. [22], is used:

$$R(z) = \rho\, exp^{-2\mu_{eff}z} \tag{1}$$

where

$$\begin{cases} \mu_{eff} = G(g, \mathrm{NA})\,(\mu_a + a(g)\mu_s) \\ \rho = \mu_s \Delta Z b(g, \mathrm{NA}) \end{cases} \tag{2}$$

Here, ρ is the fraction of the light backscattered from the focus into the collection angle of the LC-OCT objective; $\mu_a(\lambda)$, $\mu_s(\lambda)$, and $g(\lambda)$ are the absorption, scattering, and anisotropy coefficients; NA is the NA; ΔZ is the axial resolution of the imaging system; and $G(g, \mathrm{NA})$, $a(g)$, and $b(g, \mathrm{NA})$ are the model parameters described in reference [22]. $G(g, \mathrm{NA})$ takes into account the average photon path length considering the NA of the imaging system and the anisotropy factor g of the sample. For the LC-OCT setup used in this study, G was set to 1 (for NA = 0.5) [22]. $a(g)$ reflects the possibility of photon to reach the focus in highly forward scattering media despite multiple scattering. For cases of isotropic scattering, $a(g)$ is close to 1, while for highly forward scattering medium $a(g)$ tends forward 0. This parameter describes the slowed down attenuation of light with depth by the so-called serpentine phantoms [23]. $0 \leq b(g, \mathrm{NA}) \leq 1$ is the fraction of light that is scattered within the focus in such a way that it can be collected by the LC-OCT objective lens. It is ruled by the phase function of the sample and the NA of the imaging system [22]. The factor 2 in Equation 1 accounts for the round-trip light attenuation by the sample. Since scattering in most biological tissue dominates over absorption ($\mu_s >> \mu_a$), the role of absorption was neglected in this study [14].

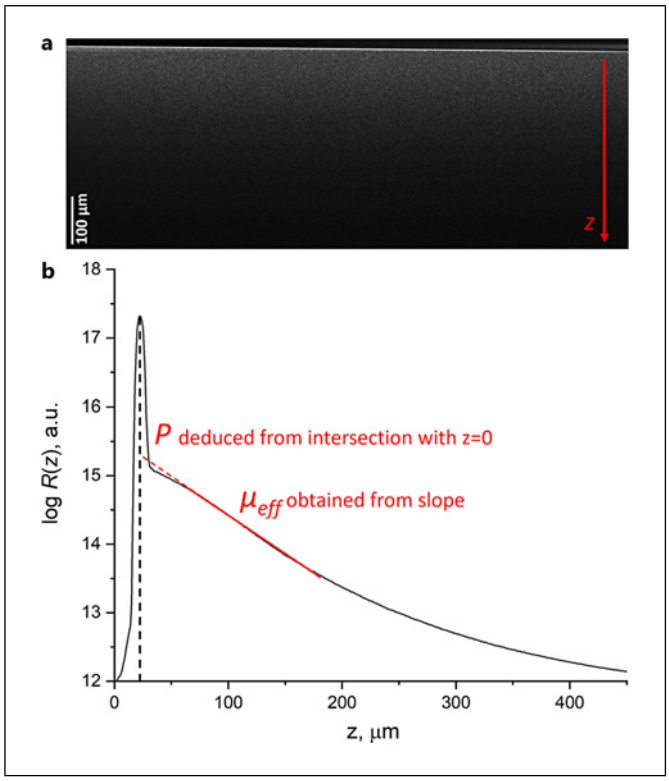

Fig. 1. a LC-OCT cross-sectional image of a liquid phantom including ILs in a logarithmic intensity scale. **b** Averaged intensity profile $R(z)$, showing mean linear regression fit of liquid phantom (in red) and corresponding observables (ρ, μ_{eff}). The observable ρ in the figure is indicated by a capital *P*.

In this model, μ_{eff} and ρ parameters are the experimental observables. To deduce optical properties at the center wavelength λ = 800 nm – $\mu_s(\lambda_{800})$ and $g(\lambda_{800})$, the observables are extracted from 3D LC-OCT images by applying a linear regression fit to the mean intensity profile (shown in Fig. 1) and then mapped to the model described by Equations 2 and 3. A calibration step, used to convert a mean intensity profile $I(z)$ into reflectance $R(z)$ (to make LC-OCT images suitable for Jacques' model), is described in reference [23, 24].

For each phantom, the fitting boundaries were defined manually, focusing primarily on the linear sections of the attenuation slope before it is significantly influenced by the background of multi-scattered light, which alters the behavior of the slope. In each 3D LC-OCT image, a linear fit was performed over 100 iterations, adjusting the fit boundaries in 10-µm increments with a step of 1 µm. This approach was used to assess the variability in the fitting process based on the selected fitting range. Finally, the bulk optical properties obtained were averaged from 5 LC-OCT images acquired for each phantom.

Optical Spectroscopy for Fluorescence and AF Spectra Acquisition on Liquid Phantoms and Human Skin Models, Respectively

The SpectroLive® device was used to acquire spatially resolved DR and multiply excited fluorescence spectra. For more details on technical and metrological features, refer to references [27, 28]. Briefly, the probe utilized a central excitation fiber (600-µm core diameter, NA = 0.22) to deliver light to the phantom surface, surrounded by four concentric rings of six collection fibers each (200-µm core diameter, NA = 0.22). The collection fibers were positioned at source-detector separations (SDSs) of 400 µm (D1), 600 µm (D2), 800 µm (D3), and 1,000 µm (D4). Sequential fluorescence emission spectra were recorded using five LED sources with bandpass filters (FWHM ~ 10 nm) centered at wavelengths $\lambda1$ = 365 nm, $\lambda2$ = 385 nm, $\lambda3$ = 395 nm, $\lambda4$ = 405 nm, and $\lambda5$ = 415 nm. For DR spectra, a broadband xenon flash lamp (350–800 nm) was employed. The fluorescence and DR spectra were captured using four HRS-BD1 spectrometers (Mightex, USA), covering a spectral range of 350–800 nm with optical resolutions of 1.7, 4.1, 4.1, and 9.7 nm FWHM for D1, D2, D3, and D4, respectively.

Since the position of the excitation peak of Ce6 is located almost at excitation wavelength λ_4 (405 nm) of SpectroLive device, the results part of this article will focus mainly on the fluorescence signal obtained using this excitation wavelength. For each phantom, spectra were acquired 3 times at 3 random surface positions of liquid phantoms to improve signal-to-noise ratio.

The raw intensity spectra obtained from the spectrometers were initially processed using a median filter to remove any high-amplitude spike artifacts. Following this, a background spectrum (collected the same day with the light sources turned off) was subtracted from all measurements. The resulting background-corrected spectra were then smoothed using a Savitzky-Golay polynomial filter with a spectral window of 20 nm. For the fluorescence spectra, these processed data were further adjusted by normalizing with specific spectral correction coefficients to account for the variations in the transfer function of each detection channel. Finally, the spectra were scaled by the incident illumination power to ensure consistent amplitude comparison using a standardized relative intensity scale (in arbitrary units).

Final data analysis consisted in extraction of peak amplitudes, corresponding to the fluorescence emission

of Ce6. MATLAB software (R2023b, The MathWorks) was used for all spectral data preprocessing functions. Obtained fluorescence amplitudes were averaged for each phantom.

Liquid Optical Phantoms

Phantoms Prepared to Compare μ_s and g Values Obtained by DIS and LC-OCT

In order to compare μ_s and g values obtained from DIS and LC-OCT techniques, a first set of 5 liquid phantoms was developed including 0.0033% (vol./vol.) of India Ink (Ref. 45807073, Lefranc & Bourgeois, France) and Intralipid® (IL) 20% (Ref. I141-100 ML, Sigma-Aldrich, St. Louis, MO, USA) in different concentrations: 1, 3, 6, 9, and 12% (vol./vol.) India Ink and ILs were chosen as absorber and scatterer, respectively, since they are commonly used in scientific literature to obtain biological tissues' typical absorption and scattering coefficients [14, 29].

Phantoms Prepared to Evaluate Impact of Modified Scattering (Measured by LC-OCT) on Fluorescence Measurement (by Optical Spectroscopy)

A set of 9 phantoms was prepared for LC-OCT and spectroscopic measurements containing 0.0033% (vol/vol) of India Ink, 20% IL in three different concentrations (1, 6, and 12% [vol/vol]), and 90-μM solution of Ce6 fluorophore (Ce6, Ref. POR0001, Advanced BioChemicals, USA) in 3 different concentrations; 2, 8, and 16% (vol/vol). To prevent possible sedimentation of particles, all solutions were placed in an ultrasonic bath for 10 min and a magnetic stirrer was used to homogenize liquid phantoms prior to measurements.

In vitro-Grown 3D Human Skin Models

To support the results obtained in this study on liquid homogeneous phantoms, complementary measurements were performed in a modality in which it would be possible to observe changes in the fluorescence signal of the same sample with changes in its optical properties. The Phenion full-thickness (FT) model (Henkel, Germany) was used as a multilayered model of real human skin featuring a epidermal and dermal layers, separated by a basal membrane. Typical sample of such tissue has a diameter of 1.3 cm and comprises keratinocytes and fibroblasts derived from a single human donor [30]. Upon delivery, the tissue samples were processed according to the manufacturer's guidelines. Immediately after receipt, each Phenion model specimen was transferred from its shipping plate into a 3.5-cm Petri dish lined with filter paper and filled with 4–5 mL of pre-warmed culture medium (37°C, Air-Liquid Interface Medium). The tissues were incubated overnight at 37°C before being used for the further manipulations.

To (reversibly) modify the optical properties of Phenion FT sample, the OC technique was used. It involves the use of special chemicals called optical clearing agents (OCAs), which may permeate within the tissue making it more optically transparent. More detailed information about this method can be found in various scientific publications [28, 31]. In this study, one OCA mixture was chosen based on our own preliminary study [28]. It was made of polyethylene glycol 400 (Ref. 202 398, Sigma-Aldrich) and DMSO (Ref. 276 855-1 L, Sigma-Aldrich): volume fractions were 80% and 20% (vol/vol), respectively. Refractive index of OCA was measured as 1.466 using Abbe refractometer DR-M2/1550 (Atago, Japan) at 480 nm and at room temperature (24°C).

Following the application of small amount of OCA (<1 mL) on the surface of Phenion model, it was gently massaged onto the sample for 1 min. After this, the sample was placed in contact under the LC-OCT probe and images were taken for 90 min every 5 min. Also, fluorescence spectra were acquired at 2 timepoints (before and after clearing: 0 and 90 min) to not disrupt the sample position under the LC-OCT probe used for scattering coefficient and anisotropy factor estimation. The same protocol was applied to one Phenion FT sample with phosphate buffer saline (PBS) used as control instead of OCA. Besides the data processing described above in the text for LC-OCT images and fluorescent spectra, the thickness of the stratum corneum (SC) and the underlying epidermis at each time point were estimated for Phenion samples based on OCT images by measuring 10 evenly distributed points over the surface of the sample. Also, bulk optical properties of epidermis and dermis were estimated from LC-OCT images separately, taking into account the attenuation correction for the bottom layer, which is described in detail in references [23, 24]. Finally, instead of exogenous fluorescence peak, here the AF peak has been analyzed. To eliminate the influence of possible fluctuations in a narrow spectral range, the area under the curve was calculated for the spectral range of AF peak position ±10 nm.

Results and Discussion

Liquid Phantoms

Bulk optical properties measured at $\lambda = 800$ nm (center wavelength of LC-OCT technique) estimated by LC-OCT-based approach and by DIS and IAD method for each liquid phantom featuring varying concentrations of

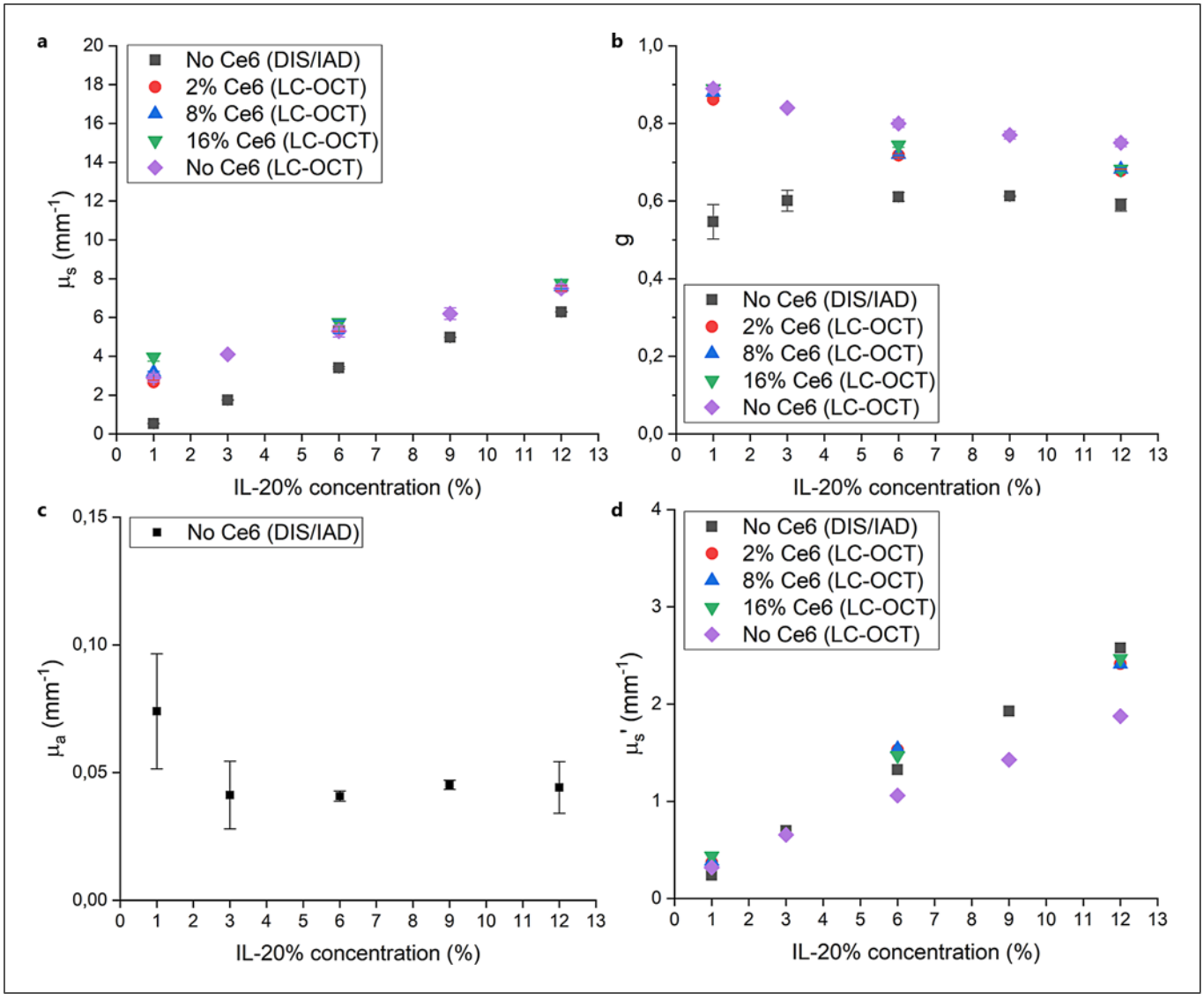

Fig. 2. a, **b** Graphs of bulk scattering properties (scattering coefficient μ_s and anisotropy factor *g*) of liquid optical phantoms containing 20% IL and Indian ink, at λ = 800 nm (central wavelength of LC-OCT imaging technique), estimated by both LC-OCT-based approach and DIS/IAD method as a function of 20% IL concentration (%, vol/vol) for each of 9 fluorescent phantoms (with varying [%, vol/vol] concentration of 90 μM solution of Ce6) and 5 phantoms without Ce6. **c** DIS/IAD estimated absorption coefficient of liquid IL phantoms as a function of 20% IL concentration (%, vol/vol). **d** Resulting scatterplot of reduced scattering coefficient μ_s'. SD bars represent the variation between the measurements on the same sample.

Ce6 fluorophore and ILs are shown in Figure 2. Figure 2a shows that the Ce6 fluorophore does not have any impact on the scattering coefficient measurement. This means that Ce6 does not scatter light; it behaves like a pure fluorophore (or like a pure absorber of the excitation wavelength) at least on the spectral range under study (800 nm) and at the concentrations tested (0–16%). For all Ce6 concentrations, whatever the IL concentration under consideration, μ_s falls within the same average value (within the standard deviation [SD]) when measured by LC-OCT. Scattering properties are well within the typical range observed for skin tissues: $\mu_s(\lambda_{800})$ values range from 0.5 to 6 mm^{-1} corresponding to 1% and 12% IL concentrations, respectively (shown in Fig. 2a) when measured with DIS-optical bench. Kono et al. provided mean values of $\mu_s(\lambda_{800})$ measured on 198 Japanese people ranging from 7.5 to 9.5 mm^{-1} depending on body site (finger and inner forearm, respectively). Therefore, a 12%

IL concentration seems to better mimic the scattering coefficient of skin tissues. However, ILs tend to provide a low *g* value as it is quite constant for all IL concentrations around 0.6 when measured with DIS-optical bench (shown in Fig. 2b). Such a value is lower than typical *g* values estimated for skin tissues at 800 nm: 0.75 [14]. However, ILs seem to be a good material to mimic the reduced scattering coefficient (μ_s') of biological tissues: when measured with DIS, this coefficient ranges from 0.2 to 2.5 mm^{-1} for 1% IL and 12% IL phantoms, respectively. The reduced scattering coefficient measures how much light is scattered by tissue assuming equal probability for the scattering angle (isotropic scattering) [32]. Reduced scattering coefficient can be formulated as follows: $\mu_s' = \mu_s \times (1 - g)$ with μ_s as the scattering coefficient, a measure of how much light is scattered per unit distance when considering single scattering; and *g* as the anisotropy factor, describing the degree of forward versus backward scattering of light. The mean value of μ_s' measured in vivo by spatial frequency domain imaging at 851 nm on 15 subjects was reported to range from 1.28 mm^{-1} (on cheek) to 1.65 mm^{-1} (on forearm). In this case, the 6% IL phantoms would better mimic typical biological tissues with a reduced scattering coefficient ($\mu_s' = 1.4\ mm^{-1}$) measured with the DIS-optical bench.

If the scattering events are independent and dilution with the matrix (and absorbing dye or fluorophores) does not influence the optical properties of the single scattering particles, μ_s and μ_s' follow a linear increase (through the origin) with increasing IL concentration; under these conditions, the anisotropy coefficient is independent of the IL concentration. However, if the concentration of IL is higher than 1%, individual scattering events can influence each other. This phenomenon is often referred to as dependent or correlated scattering [33]. Zaccanti et al. [34] studied the bulk scattering properties (μ_s, μ_s', and *g*) at 633 nm for several IL dilutions with a volume fraction up to 0.227 mL/mL (pure IL). Both μ_s and μ_s' followed a second-order polynomial as a function of volume fraction, while *g* followed a nearly linear decrease. Measurements made by LC-OCT shown in Figure 2b follow the same decreasing trend. The values measured by the DIS-IAD method seem more stable for concentrations below 9% and decrease for higher IL concentrations: *g* measured for the 12% IL concentration is smaller than *g* measured for the 9% IL concentration.

Comparison of μ_s and *g* Values Obtained by DIS and LC-OCT

Considering the DIS and IAD approach as the gold standard for scattering coefficient measurement, the differences observed between the two approaches for the corresponding IL concentrations (shown in Fig. 2a) show that LC-OCT overestimates $\mu_s(\lambda_{800})$: for the 9% IL concentration, $\mu_s = 5\ mm^{-1}$ and $6\ mm^{-1}$ when measured by DIS and LC-OCT, respectively, which corresponds to a 20% overestimation of μ_s by LC-OCT compared to DIS. According to observations made by Waczczuk et al. [23] such a difference is due to the uncertainties introduced by the application of Jacques model, as well as the uncertainties caused by measurements on a calibration phantom. Indeed, LC-OCT device includes a silicone immersion oil featuring a refraction index value $n = 1.4$. Liquid phantoms used in the current study are made of distilled water as the main diluting liquid which implies that they feature $n = 1.33$. This refractive index shift will induce a shift in the focal plane of the microscope objective and therefore in the plane corresponding to the zero-path difference of the interferometer. This will result in a faster signal decay than the decay according to Beer-Lambert's law and eventually to overestimation of optical coefficients. Besides, additional factors such as possible sedimentation and aggregation of particles in liquid phantoms should be taken into account, despite numerous measures in this experimental protocol aimed at preventing this: an ultrasonic bath was used to break aggregated particles, and magnetic stirring was used to avoid sedimentation. Each method does perform measurements on the same liquid phantoms, but the measurement process considers each sample in very different ways: 10 mL of the phantom is poured into a cell culture plate well for LC-OCT measurements, while 3 mL of the liquid phantom is poured in a 1-mm-thick sample holder. Therefore, the dependent scattering event might happen more frequently in the configuration of LC-OCT measurements than for the DIS-IAD measurement. This might explain the different trends observed for concentrations under consideration.

Measuring the scattering coefficient of biological samples (in vivo or ex vivo) has been the subject of numerous studies in recent years, using different techniques, different spectral ranges, different assumptions (on the anisotropy factor *g* and refractive index *n* values), and different data processing methods or approach (skin being considered either as a single layer or as two distinct layers: the epidermis and the dermis). This discussion on measurement variability was addressed by Lister et al. [35] in 2012 on the basis of a widely referenced set of absorption and scattering data for human skin published by Jacques et al. [36]. Interpretation of the acquired data was carried out using the diffusion approximation. Prahl [37] one of the authors of this paper, presented in his PhD thesis an almost identical process for determining

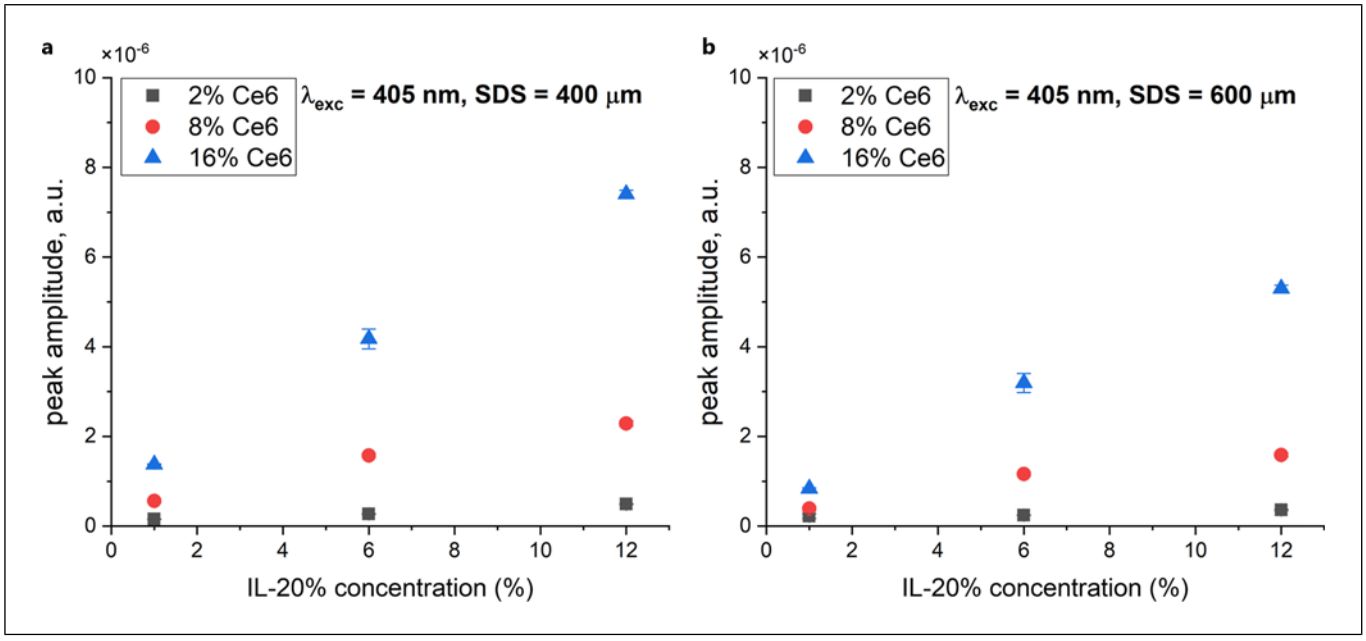

Fig. 3. Fluorescent peak amplitudes of 9 liquid optical phantoms containing 20% IL, Indian ink, and various concentrations of Ce6 (2, 6, and 12%, vol/vol) as a function of 20% IL concentration (%, vol/vol), excited at λ = 405 nm and collected by distances. **a** D_1 = 400 μm. **b** D_2 = 600 μm.

the optical properties of abdominal skin samples, but applying the IAD method. Graaf et al. [38] provided further analysis of Prahl's data using a Monte Carlo technique. The reduced scattering coefficients calculated in these studies range from 5.3 to 18.7 mm^{-1} at 633 nm, corresponding to a variation of 268%. This demonstrates that an alternative analysis of the same data can lead to a wide range of optical coefficient estimates. More recently, in vivo measurements were performed by Phan et al. [39] using spatial frequency domain imaging and by Kono et al. [40] using reflection spatial profile measurement on cheek and ventral forearm. Kono et al. measured μ_s = 8 and 9.5 mm^{-1} on cheek and ventral forearm, respectively, at 800 nm; Phan et al. measured μ_s' = 1.53 and 1.46 mm^{-1} (assuming g = 0.9), leading to μ_s = 15.3 and 14.6 mm^{-1}, respectively, at 851 nm. In this case, the variation is greater than 60% when the scattering coefficient is estimated using two different techniques. Compared with such variations, the 20% discrepancy between the scattering coefficient estimated by LC-OCT and DIS seems acceptable.

However, the results calculated in the current study for the reduced scattering coefficient $\mu_s'(\lambda_{800})$ (shown in Fig. 2d) give closer results which indicates that the uncertainties on μ_s and g compensate for each other as they probably arise from the same numerical origins: $\mu_s'(\lambda_{800})$ values overlap for low-scattering phantoms and feature a maximum 20% difference for the 12% IL concentrated phantom, when estimated by the two methods used (LC-OCT versus DIS/IAD). The absorption coefficient $\mu_a(\lambda_{800})$ (shown in Fig. 2c) is significantly lower than the scattering coefficient and remains constant despite increasing IL concentration, which confirms the ability of the DIS-optical bench to measure absorption coefficient independently of the scattering coefficient. Welch's ANOVA test was applied to $\mu_a(\lambda_{800})$ values to determine whether changes in IL concentration have a significant impact on the absorption coefficient: for all groups tested pairwise, differences of absorption coefficient are not significant ($p > 0.05$). For both methods (LC-OCT and DIS/IAD), an increase in IL concentration leads to a higher $\mu_s(\lambda_{800})$ value, which is consistent with predictions from Mie theory. Adding Ce6 (0–16%, vol/vol) does not modify the scattering coefficient μ_s: scattering coefficient values obtained by LC-OCT method on phantoms including Ce6 fluorophore or not are the same regardless the 20% IL concentrations (shown in Fig. 2a). LC-OCT therefore provides a unique means of evaluating scattering optical properties μ_s and g separately, while enabling these properties to be assessed noninvasively on in vivo samples.

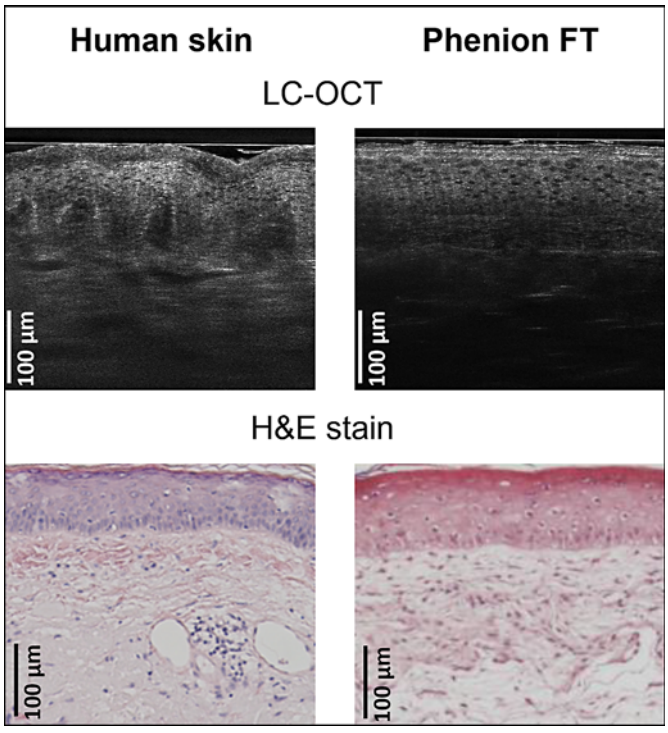

Fig. 4. Comparative illustration of human skin (left column) and Phenion FT artificial skin (right column): LC-OCT images (top) and H&E-stained histological images (bottom). LC-OCT, line-field confocal optical coherence tomography; Phenion FT, Phenion full-thickness skin models; H&E, hematoxylin and eosin.

Impact of Modified Scattering on Fluorescence Measurement of Liquid Phantoms

Measurements of Ce6 fluorescence intensity at an excitation wavelength of 405 nm (corresponding to the absorption maximum of Ce6) are shown in Figure 3 for 2 distances between excitation and fluorescence detection: 400 and 600 µm (SDS) for each of the three IL concentrations (1, 6, and 12%) and Ce6 concentrations: 2, 8, and 16%. Ce6 fluorescence intensity increases as IL concentration increases for all three Ce6 concentrations, with a slope that increases along with Ce6 concentration. A longer distance between fluorescence excitation and collection (shown in Fig. 3b) results in a decrease in measured fluorescence intensity. This decrease in the measured intensity is due to the average pathlength of photons in phantoms which is longer when the photons are detected by the collection fiber located at 600 µm than by the collection fiber located at 400 µm from the excitation fiber. When the average pathlength of photons is longer, they statistically have more chance of being scattered or absorbed and therefore of not being detected by the fiber located at 600 microns.

Such an increase in measurements of fluorescence intensity has already been reported by Alghourani et al. [41]: protoporphyrin IX fluorescence (using a 405-nm excitation wavelength) increased (635-nm peak intensity ×1.4; ×1.8; ×1.6; and ×1.9) as scattering coefficient increased from 5 to 30 mm^{-1} (×2; ×2; ×1.5; and ×3, respectively). In order to mimic biological tissues' scattering properties, the scattering coefficient range used in the current study was lower than the range used by Alghourani et al. [41]: DIS-optical bench measured μ_s = 0.5, 3.5 and 6 mm^{-1} for 1, 6, and 12% IL concentrations, respectively. For the 16% Ce6 concentration, fluorescence intensity increased (×3.5, ×1.8, and ×6.2) as scattering coefficient increased: ×7.6, ×1.6, and ×12, respectively. As a general observation, increase in scattering coefficient induces an increase in the measured fluorescence intensity but in a lower proportion. It is to be noticed that Chen's team reported [42] an opposite observation to the two just previously described: for IL concentrations (100 times lower concentrations than the ones used in the current study), fluorescence intensity (of Fura-2 pentapotassium salt using ultraviolet excitation and fluorescence intensity recorded at 510 nm) decreased, i.e., was divided by a factor 2 for 0% compared to 0.06% IL concentrations. Interactions of ILs with fluorophores depend on each compound's chemical properties resulting in specific interactions that could explain opposite observations presented in different studies.

In vitro-Grown 3D Skin Models

Skin Models' Histological and Optical Properties

In vitro-grown skin Phenion FT models are supposed to be an experimental substitute for human skin in optical experiments, since they are generally structurally identical to skin. This is shown in Figure 4 showing histological images (bottom row) and LC-OCT images (top row) of human skin (left column) and Phenion FT models (right column). The structure of Phenion FT samples is similar to human skin in terms of morphology (the layered structure is observed, including the SC, several layers of living epidermis, the basement membrane or dermoepidermal junction, and the dermis located underneath). Also, the thickness of the Phenion FT epidermal layers (mean SC thickness was measured as 17 ± 10 µm, the rest of epidermis – 153 ± 24 µm, depending on the sample) is comparable to those of human skin (typical SC thickness is reported to be around 20 cell layers or 20 µm with the total epidermal thickness ranged from 75 to 150 µm) [43]. The main difference observed is in the dermoepidermal junction, which is smooth and flat in Phenion FT, whereas

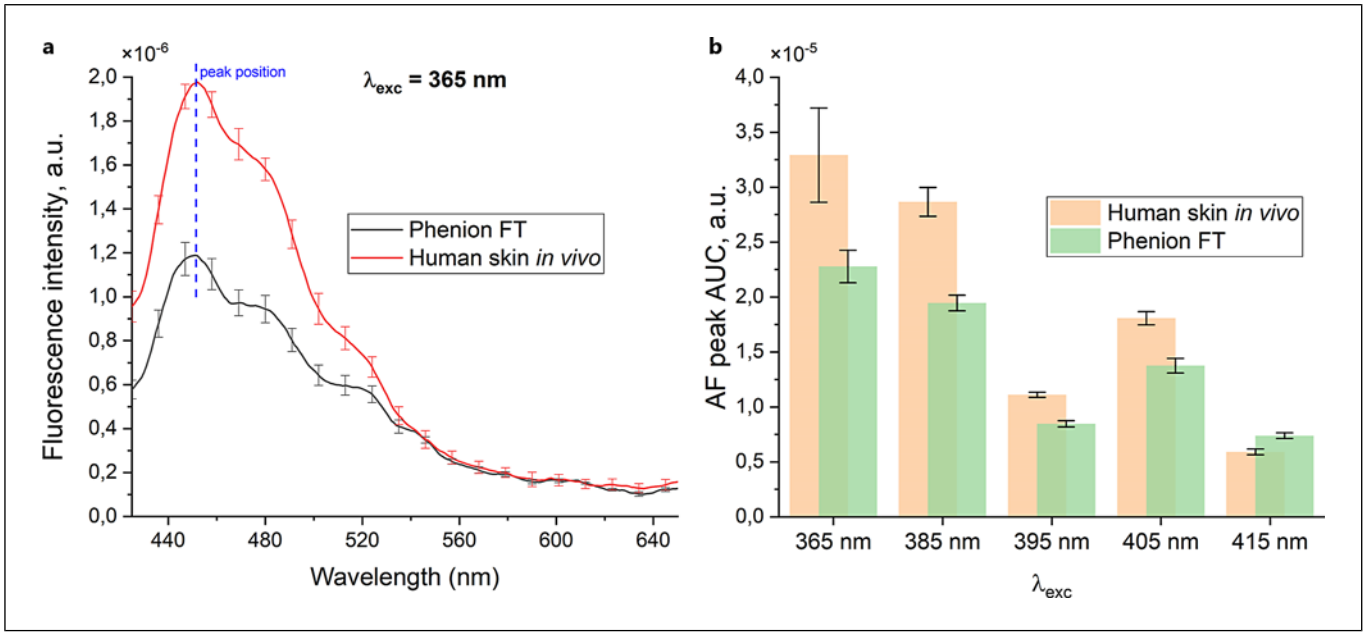

Fig. 5. a AF spectra of human skin acquired in vivo (red curve) and on in vitro-grown 3D Phenion FT model (black curve) using 365-nm excitation and recorded at the 400-μm SDS. **b** AF peak AUC 5 different excitation wavelengths (λ_{exc}) for AF measured on human skin in vivo and on in vitro-grown 3D Phenion FT model. Error bars correspond to the SD of 3 measurements on adjacent areas of the sample (with 3 acquisitions on each area resulting in total of 9 spectra), keeping optical probe in gentle contact with skin surface (in vivo or on skin models). AUC, area under the curve.

it may be curved and papillary in human skin, depending on skin sites. It is also worth noting that, despite an epidermis thickness similar to that of human skin, the differences in thickness of the SC and the rest of the epidermis between the different Phenion samples are quite significant (the SD for the SC is greater than 50% of the mean, and the SD for the epidermis is greater than 15% of the mean), making it difficult to use Phenion FT samples for any kind of experimental statistics.

Spectral comparison of human skin in vivo (ventral wrist) and Phenion FT is shown in Figure 5. It can be seen that the AF spectra (shown in Fig. 5a) excited at a 365-nm wavelength and recorded at the 400-μm source to detector distance (SDS) are similar in shape as well as in peak position (451 nm), related to the contributions of collagen and NAD(P)H. However, the AF spectrum of skin features a higher intensity throughout the observed range, which is probably due to the difference in the biochemical composition of the samples: higher concentration of fluorophores in skin than in the Phenion FT model. This is also shown in Figure 5b, which displays the peak intensity area under the curve (peak position ± 10 μm) of AF peaks upon excitation at different wavelengths for the 400-μm source to detector distance.

Impact of Clearing-Induced Changes in Scattering Properties on AF Measurements in Skin Models

As shown in Figure 6, OC induced an increase in Phenion FT fluorescence spectra. For further analysis, only spectra excited at 365 nm and collected at an SDS (SDS1) of 400 μm were used.

The kinetics of the scattering coefficient and anisotropy factor of Phenion FT artificial skin, as well as changes in thickness and AF signal (resulting from OC), are shown in Figure 7. At initial LC-OCT image, SC layer of Phenion FT model is clearly seen (shown in Fig. 7c, left), while after OCA exposure it is almost non-traceable (shown in Fig. 7c, right). Also, there is a visible reduction in the epidermal thickness, which in turn caused improved contrast of underlying dermal structures.

Combining μ_s and g values (shown in Fig. 7a, b) to obtain the reduced scattering coefficient using the formula $\mu_s' = \mu_s \times (1 - g)$, $\mu_s' = 4.95$ mm^{-1} for control epidermis, which is comparable to the value provided by Shimojo et al. [44]: 3.98 ± 1 mm^{-1} obtained for a wavelength of 800 nm on 15 ex vivo human skin samples using the DIS method. This confirms once again that such skin models feature optical properties comparable to those measured in vivo.

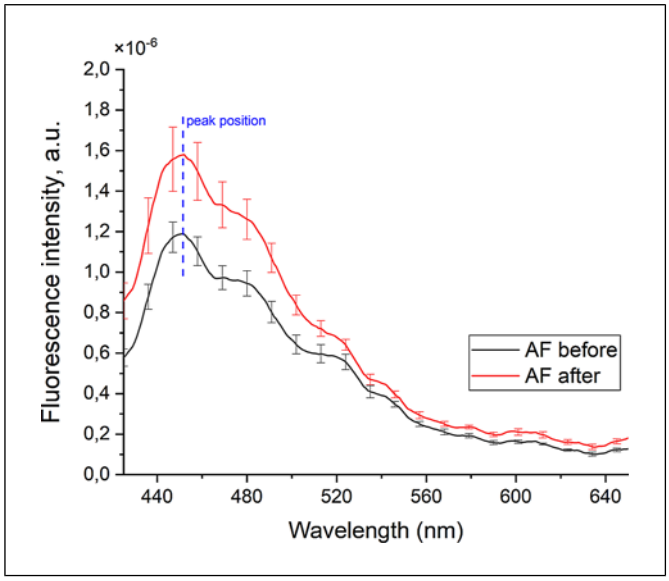

Fig. 6. AF spectra (in a.u.) acquired on Phenion FT model before (black curve) and after (red curve) OC, excited with 365-nm wavelength and recorded at the 400-μm source to detector distance (SDS1). a.u., arbitrary units.

OC results in a ~21% decrease in the epidermal anisotropy factor, whereas for the PBS control this decrease is ~11% (shown in Fig. 7b) while the scattering coefficient features an increase of 10% (shown in Fig. 7a), comparable to the control (~15% increase). Dermal layer scattering coefficient features a strong increase induced by OC compared to the PBS control: ~67% increase after 40 min of OCA diffusion vs. ~26% increase for the PBS control. Since the OCA mixture did not induce any decrease of dermis scattering properties, it might mean that the OCA did not penetrate down to the dermis, below the epidermis layer. This might be due to the nature of the material used to build the dermis layer, made of collagen in which fibroblasts are grown, that prevented the OCA diffusion.

A decrease in epidermal anisotropy could here indicate the noticeable dehydration of the upper layer of the Phenion FT model, caused by OCA, while the OC was not fully achieved as the μ_s coefficient for epidermis did not decrease. This is in agreement with Mie theory, according to which it is explained by a decrease in the size of the scattering particles rather than to RI matching [14, 45]. These assumptions are confirmed by the observed reduction in epidermal thickness (shown in Fig. 7c) under the effect of OCA. Two possible reasons may explain that in this case no clearing effect was observed: the osmotic effect of the PEG-400/DMSO mixture and the probe pressure effect applied to the sample. We previously reported this observation in our earlier studies on ex vivo human skin samples to be responsible for induced compaction (thickness modifications) of cutaneous layers and corresponding changes in spectral measurements [28].

Dermal scattering increase is another surprising behavior observed here, as the typical effect of OC on skin is a decrease in scattering [31]. Considering the thickness decrease (which is more pronounced as compared to PBS control, for which SD bars overlap), a higher scatterer concentration per unit volume is the possible explanation, which could be as well related to dehydration caused by OCA. However, it is shown in Figure 7d that skin AF signal has increased by ~35% after OC (versus ~22% increase for control). On the one hand, this contradicts the indirectly observed results of dehydration, since the recorded AF of biological tissues is directly proportional to the hydration of the samples, due to the fact that the temperature and pH of tissues (variables that directly affect fluorescence) are changed with dehydration [14]. On the other hand, as is known from other works [41] and from our own results (shown in Fig. 3), the registered fluorescence is directly proportional to the scattering coefficient, which is associated with the probability of photon absorption by the fluorophore. In this case, the excitation wavelength of 365-nm well excites collagen present in various forms in biological tissues [46]. Thus, a decrease in the thickness of the epidermis, which allows excitation photons to better penetrate the dermis (the main collagen-containing layer) and return to the collecting fiber of the spectral probe, and an increase in the scattering of the dermis layer compensate for dehydration and allow to observe an increase in the registered AF signal. Moreover, as shown in Figure 7, even for the control condition such a decrease in sample thickness caused an increase in the registered AF signal, albeit on a smaller scale. With the absence of OCA effect, the only possible reason was the probe pressure effect applied to the sample, which was reported in our earlier studies on ex vivo human skin samples to be responsible for induced compaction (thickness modifications) of cutaneous layers and corresponding changes in spectral measurements [28]. Finally, it should be mentioned again that Phenion FT skin models vary a lot in epidermis and SC thicknesses from sample to sample, hampering the influence of experimental protocol influence on the data obtained.

As a result, the main observed result – an increase in the registered fluorescence with an increase in the scattering of the Phenion skin model – correlates well with the results demonstrated on liquid IL phantoms. These results open up prospects for further research aimed at

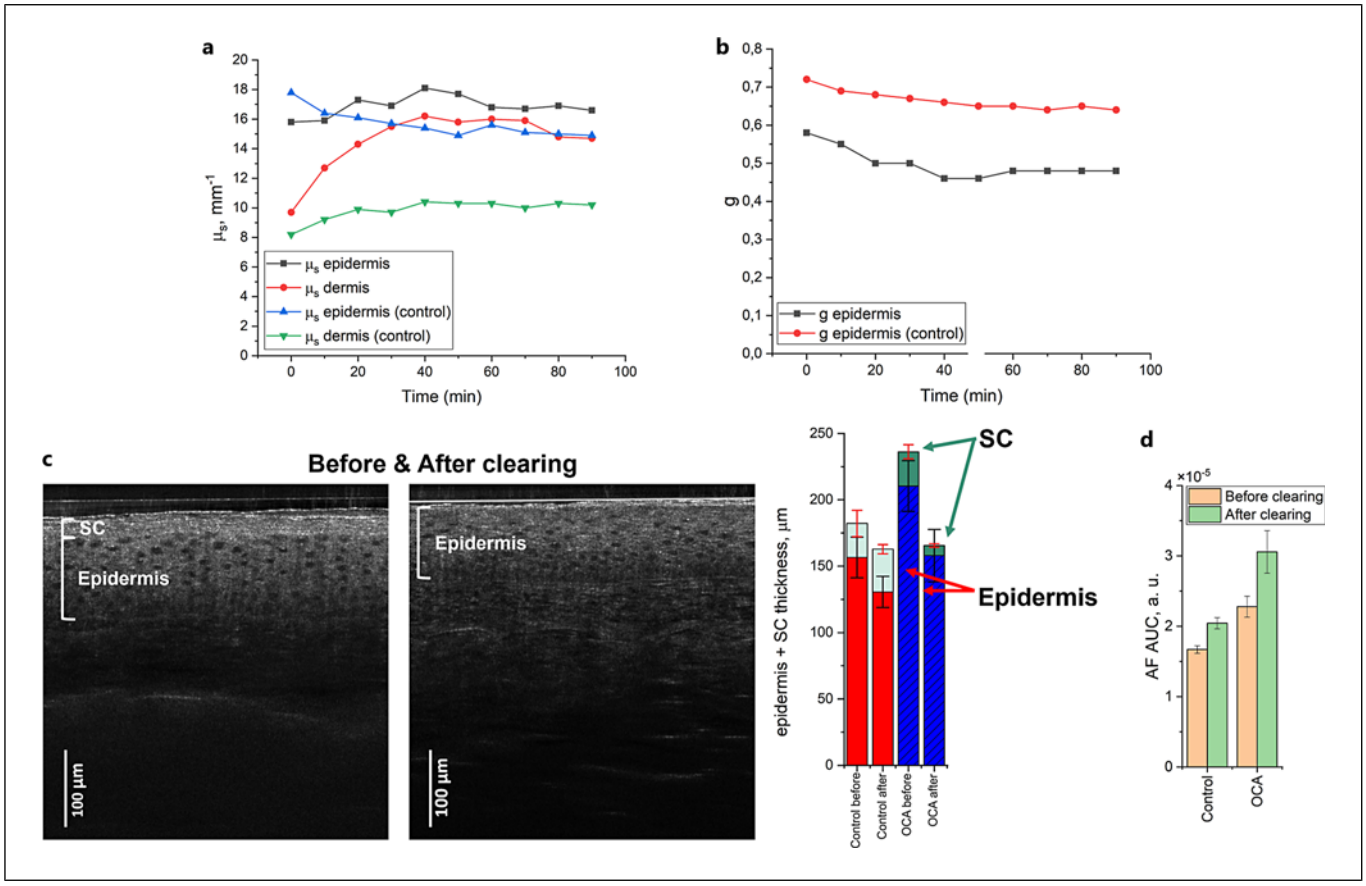

Fig. 7. Scattering coefficient μ_s (**a**) and anisotropy factor g (**b**) kinetics at λ = 800 nm of Phenion FT artificial skin model layers as a function of OC duration (and control using PBS), estimated from LC-OCT images. **c** Illustrative B-scans of LC-OCT images of Phenion FT sample before and after clearing and its layer-wise thickness change histogram, comparing sample before and after clearing (blue bars) and before and after control using PBS (red bars). **d** AF peak amplitude (excited by λ = 365 nm and collected at 400-μm distance), calculated as AUC for peak position ± 10 nm, comparing intact spectral measurements and the measurements after clearing with clearing control using PBS. SD bars represent variations between multiple measurement positions. AUC, area under the curve; SC, stratum corneum; SD, standard deviation.

noninvasive determination of fluorophore concentrations in biological tissue samples and their pathology-related modifications based on the simultaneous registration of fluorescence spectra and LC-OCT-based estimation of bulk scattering properties. Some studies have already put forward semiempirical models describing the fluorescence signal of turbid media as a function of the scattering properties of the medium [16]. However, the possibility of assessing in vivo the optical properties of tissues and their effect on fluorescence, investigated in the present study, opens up new prospects in this direction. Whether based on deep learning methods (convolutional neural network [47]) or experimental modeling methods [42] (using calibration phantoms), several previously published solutions could be tried to correct the data and obtain corrected fluorescence spectra. However, since the results depend on specific compounds of the phantom or on skin model, a dedicated study should be the next step to address the results obtained during the current study.

Conclusion

In this paper, the μ_s and g bulk scattering properties (at 800 nm) of liquid fluorescent phantoms composed of Ce6, 20% IL, and India Ink were estimated separately as a function of IL concentration from LC-OCT images using linear regression of the depth reflectance profile and a modified model based on the Beer-Lambert law. These results were then compared with values obtained with

DIS and separate recording of collimated transmittance spectra followed by IAD estimation of bulk scattering properties. Although LC-OCT overestimates the values of both μ_s and g (up to 20% for μ_s and around 30% for g), this technique provides a good approximation of the reduced scattering coefficient (underestimation of 16% for the 6% IL phantom) and features the strong advantage of being useable in vivo.

Changes in the amplitude of the Ce6 fluorescence peak were measured as a function of IL concentration using fluorescence spectroscopy, showing the linear dependence of the fluorescence intensity measurement on increasing scattering coefficient. The results obtained on phantoms were then validated with the in vitro-grown skin model, where an OCA-induced increase in dermal scattering was observed using the LC-OCT approach, while spectral measurements demonstrated a corresponding increase in collagen AF signal. Besides these results, comparison of the AF signal collected on these human skin models with the AF signal collected on human skin in vivo confirmed that such models include all endogenous fluorophores in the same proportions as those expressed by human skin. The present study demonstrates the ability of two optical devices to measure both scattering coefficient and fluorescence: the combination of these two devices could potentially enable future in vivo application to obtain information on pathology-related modifications in skin fluorophore concentration.

Statement of Ethics

This study was performed in accordance with the Declaration of Helsinki. This human study was approved by Comité de Protection des Personnes CPP Est III – approval: 06/09/2016. The study's clinical trial registration number is NCT02956265 registered with ClinicalTrials.gov, https://clinicaltrials.gov/study/NCT02956265?cond=Skin%20Carcinoma&term=spectrolive&rank=1. Participant registration took place from November 2016 to March 2021. All adult participants provided written informed consent to participate in this study. Written informed consent was obtained from the individual(s) for publication of the details of their medical case and any accompanying images.

Conflict of Interest Statement

Dr. Jonas Ogien is an engineer employed by DAMAE Medical company. Pr. Arnaud Dubois is the coinventor of the LC-OCT technology patent and is cofounder of DAMAE Medical company. The remaining authors have no conflicts of interest to declare.

Funding Sources

This research was carried out with the support of the French National Research Agency (ANR) under the French PIA project "Lorraine Université d'Excellence" (ANR-15-IDEX-0004-LUE) that was involved in study design. This study was part of the Spec-LCOCT project funded by the ANR (ANR-21-CE19-0056) that was involved in study design, execution, analysis, manuscript conception, planning, writing, and decision to publish. The study was carried with the DeepLive™ device of the PhotoVivo platform, which is part of the France Life Imaging (FLI: ANR-11-INBS-0006) network and funded by Contrat de Plan Etat-Région Grand Est 2015-2020 (CPER IT2MP: *Innovations Technologiques, Modélisation et Médecine Personnalisée*) thanks to the financial support by European Regional Development Fund (ERDF), Grand Est Region and Ligue Contre le Cancer that all were involved in the study execution.

Author Contributions

Sergey M. Zaytsev was involved in methodology, investigation, data processing, formal analysis, and writing – original draft, review, and editing. Marine Amouroux was involved in conceptualization, methodology, formal analysis, writing – review and editing, and project management. Walter Blondel, Jonas Ogien, and Arnaud Dubois were involved in reviewing, editing, and fund raising. All authors have read and agreed to the published version of the manuscript.

Data Availability Statement

The data that support the findings of this study are not publicly available due to privacy reasons but are available from the corresponding author upon request.

References

1 Narayanamurthy V, Padmapriya P, Noorasafrin A, Pooja B, Hema K, Firus Khan AY, et al. Skin cancer detection using non-invasive techniques. RSC Adv. 2018;8(49):28095–130. https://doi.org/10.1039/c8ra04164d
2 Borisova E, Pavlova P, Pavlova E, Troyanova P, Avramov L. Optical biopsy of human skin: a tool for cutaneous tumours' diagnosis. Int J Bioautomation. 2012;16(1):53–72.
3 Tuchin VV, Popp J, Zakharov V, editors. Multimodal optical diagnostics of cancer. 1st ed. Cham: Springer; 2020.
4 Ogien J, Daures A, Cazalas M, Perrot JL, Dubois A. Line-field confocal optical coherence tomography for three-dimensional skin imaging. Front Optoelectron. 2020;13(4):381–92. https://doi.org/10.1007/s12200-020-1096-x
5 Latriglia F, Ogien J, Tavernier C, Fischman S, Suppa M, Perrot JL, et al. Line-field confocal optical coherence tomography (LC-OCT) for skin imaging in dermatology. Life. 2023;13(12):2268. https://doi.org/10.3390/life13122268

6 Suppa M, Fontaine M, Dejonckheere G, Cinotti E, Yélamos O, Diet G, et al. Line-field confocal optical coherence tomography of basal cell carcinoma: a descriptive study. J Eur Acad Dermatol. 2021;35(5):1099–110. https://doi.org/10.1111/jdv.17078
7 Ruini C, Schuh S, Sattler E, Welzel J. Line-field confocal optical coherence tomography-practical applications in dermatology and comparison with established imaging methods. Technol. 2021;27(3):340–52. https://doi.org/10.1111/srt.12949
8 Mtimet L, Boussingault L, Aktas D, Fontaine M, Orte Cano C, Diet G, et al. Line-field confocal optical coherence tomography of basal cell carcinoma: a retrospective study on diagnostic performance. J Eur Acad Dermatol. 2025;39(8):1468–80. https://doi.org/10.1111/jdv.20459
9 Perez-Anker J, Soglia S, Lenoir C, Albero R, Alos L, García A, et al. Criteria for melanocytic lesions in LC-OCT. J Eur Acad Dermatol. 2024;38(10):2005–16. https://doi.org/10.1111/jdv.20079
10 Ashok PC, Praveen BB, Bellini N, Riches A, Dholakia K, Herrington CS. Multi-modal approach using Raman spectroscopy and optical coherence tomography for the discrimination of colonic adenocarcinoma from normal colon. Biomed Opt Express. 2013;4(10):2179–86. https://doi.org/10.1364/BOE.4.002179
11 Canetta E, Riches A, Borger E, Herrington S, Dholakia K, Adya AK. Discrimination of bladder cancer cells from normal urothelial cells with high specificity and sensitivity: combined application of atomic force microscopy and modulated Raman spectroscopy. Acta Biomater. 2014;10(5):2043–55. https://doi.org/10.1016/j.actbio.2013.12.057
12 Patil CA, Kalkman J, Faber DJ, Nyman JS, van Leeuwen TG, Mahadevan-Jansen A. Integrated system for combined Raman spectroscopy-spectral domain optical coherence tomography. J Biomed Opt. 2011;16(1):011007. https://doi.org/10.1117/1.3520132
13 Waszczuk L, Ogien J, Perrot JL, Dubois A. Co-localized line-field confocal optical coherence tomography and confocal Raman microspectroscopy for three-dimensional high-resolution morphological and molecular characterization of skin tissues ex vivo. Biomed Opt Express. 2022;13(4):2467–87. https://doi.org/10.1364/BOE.450993
14 Tuchin VV. Tissue optics: light scattering methods and instruments for medical diagnosis. 3rd ed. Bellingham: SPIE; 2015.
15 Aernouts B, Van Beers R, Watté R, Lammertyn J, Saeys W. Dependent scattering in intralipid® phantoms in the 600-1850 nm range. Opt Express. 2014;22(5):6086–98. https://doi.org/10.1364/OE.22.006086
16 Kanick SC, Robinson DJ, Sterenborg HJCM, Amelink A. Semi-empirical model of the effect of scattering on single fiber fluorescence intensity measured on a turbid medium. Biomed Opt Express. 2012;3(1):137–52. https://doi.org/10.1364/BOE.3.000137
17 Rehman AU, Ahmad I, Qureshi SA. Biomedical applications of integrating sphere: a review. Photodiagn Photodyn. 2020;31:101712. https://doi.org/10.1016/j.pdpdt.2020.101712
18 Prahl S. Everything I think you should know about inverse adding-doubling. [Internet]. Wilsonville: Oregon Tech; 2011 Mar [cited 2025 Mar 25]. 74 p. Available from: https://omlc.org/software/iad/manual.pdf
19 Chang S, Bowden AK. Review of methods and applications of attenuation coefficient measurements with optical coherence tomography. J Biomed Opt. 2019;24(9):090901–17. https://doi.org/10.1117/1.JBO.24.9.090901
20 Gong P, Almasian M, van Soest G, de Bruin DM, van Leeuwen TG, Sampson DD, et al. Parametric imaging of attenuation by optical coherence tomography: review of models, methods, and clinical translation. J Biomed Opt. 2020;25(4):1–34. https://doi.org/10.1117/1.JBO.25.4.040901
21 Vermeer KA, Mo J, Weda JJA, Lemij HG, de Boer JF. Depth-resolved model-based reconstruction of attenuation coefficients in optical coherence tomography. Biomed Opt Express. 2013;5(1):322–37. https://doi.org/10.1364/BOE.5.000322
22 Jacques SL. Confocal laser scanning microscopy using scattering as the contrast mechanism. In: Tuchin VV, editor. Handbook of coherent-domain optical methods: biomedical diagnostics, environmental monitoring, and materials science. New York, NY: Springer; 2013. p. 1157–71.
23 Waszczuk L, Ogien J, Pain F, Dubois A. Determination of scattering coefficient and scattering anisotropy factor of tissue-mimicking phantoms using line-field confocal optical coherence tomography (LC-OCT). J Eur Opt Soc-Rapid. 2023;19(2):39. https://doi.org/10.1051/jeos/2023037
24 Zaytsev SM, Waszczuk L, Ogien J, Dubois A, Blondel W, Amouroux M. Estimation of scattering properties modifications caused by in vivo human skin optical clearing using line-field confocal optical coherence tomography. J Biophotonics. 2024:e202400264. https://doi.org/10.1002/jbio.202400264
25 Thrane L, Yura HT, Andersen PE. Analysis of optical coherence tomography systems based on the extended huygens-Fresnel principle. J Opt Soc Am A. 2000;17(3):484–90. https://doi.org/10.1364/josaa.17.000484
26 Turani Z, Fatemizadeh E, Blumetti T, Daveluy S, Moraes AF, Chen W, et al. Optical radiomic signatures derived from optical coherence tomography images improve identification of melanoma. Cancer Res. 2019;79(8):2021–30. https://doi.org/10.1158/0008-5472.CAN-18-2791
27 Blondel W, Delconte A, Khairallah G, Marchal F, Gavoille A, Amouroux M. Spatially-resolved multiply-excited autofluorescence and diffuse reflectance spectroscopy: spectrolive medical device for skin in vivo optical biopsy. Electronics. 2021;10(3):243. https://doi.org/10.3390/electronics10030243
28 Zaytsev SM, Amouroux M, Khairallah G, Bashkatov AN, Tuchin VV, Blondel W, et al. Impact of optical clearing on ex vivo human skin optical properties characterized by spatially resolved multimodal spectroscopy. J Biophotonics. 2022;15(1):e202100202. https://doi.org/10.1002/jbio.202100202
29 Di Ninni P, Martelli F, Zaccanti G. The use of India ink in tissue-simulating phantoms. Opt Express. 2010;18(26):26854–65. https://doi.org/10.1364/OE.18.026854
30 Zöller NN, Kippenberger S, Thaçi D, Mewes K, Spiegel M, Sättler A, et al. Evaluation of beneficial and adverse effects of glucocorticoids on a newly developed full-thickness skin model. Toxicol Vitro. 2008;22(3):747–59. https://doi.org/10.1016/j.tiv.2007.11.022
31 Tuchin VV, Zhu D, Genina EA, editors. Handbook of tissue optical clearing: new prospects in optical imaging. 1st ed. Abingdon: Routledge & CRC Press; 2022.
32 Martelli F, Binzoni T, Del Bianco S, Liemert A, Kienle A, editors. Light propagation through biological tissue and other diffusive media: theory, solutions, and validation. 2nd ed.Bellingham: SPIE; 2022.
33 Di Ninni P, Martelli F, Zaccanti G. Effect of dependent scattering on the optical properties of intralipid tissue phantoms. Biomed Opt Express. 2011;2(8):2265–78. https://doi.org/10.1364/BOE.2.002265
34 Zaccanti G, Del Bianco S, Martelli F. Measurements of optical properties of high-density media. Appl Opt. 2003;42(19):4023–30. https://doi.org/10.1364/ao.42.004023
35 Lister T, Wright PA, Chappell PH. Optical properties of human skin. J Biomed Opt. 2012;17(9):90901. https://doi.org/10.1117/1.JBO.17.9.090901
36 Jacques SL, Alter CA, Prahl SA. Angular dependence of HeNe laser light scattering by human dermis. Lasers Life Sci. 1988;2(4):309–33.
37 Prahl SA. Light Transport in Tissue [PhD thesis]. [Austin]. University of Texas; 1988. p. 211.
38 Graaff R, Dassel ACM, Koelink MH, de Mul FFM, Aarnoudse JG, Zijistra WG. Optical properties of human dermis in vitro and in vivo. Appl Opt. 1993;32(4):435–47. https://doi.org/10.1364/AO.32.000435
39 Phan T, Rowland R, Ponticorvo A, Le BC, Wilson RH, Sharif SA, et al. Characterizing reduced scattering coefficient of normal human skin across different anatomic locations and Fitzpatrick skin types using spatial frequency domain imaging. J Biomed Opt. 2021;26(2):026001. https://doi.org/10.1117/1.JBO.26.2.026001

40 Kono T, Yamada J. In vivo measurement of optical properties of human skin for 450–800 nm and 950–1600 nm wavelengths. Int J Thermophys. 2019;40(5):51. https://doi.org/10.1007/s10765-019-2515-3
41 Alghourani KMK, Bachir W, Karraz G. Effect of absorption and scattering on fluorescence of buried tumours. J Spectrosc. 2020;2020:8730471–7. https://doi.org/10.1155/2020/8730471
42 Chen Y, Chen ZP, Yang J, Jin JW, Zhang J, Yu RQ. Quantitative fluorescence spectroscopy in turbid media: a practical solution to the problem of scattering and absorption. Anal Chem. 2013;85(4):2015–20. https://doi.org/10.1021/ac302815e
43 Tuchin VV. Tissue optics and photonics: biological tissue structures. J Biomed Photon Eng. 2015;1(1):3–21. https://doi.org/10.18287/jbpe-2015-1-1-3
44 Shimojo Y, Nishimura T, Hazama H, Ozawa T, Awazu K. Measurement of absorption and reduced scattering coefficients in Asian human epidermis, dermis, and subcutaneous fat tissues in the 400- to 1100-nm wavelength range for optical penetration depth and energy deposition analysis. J Biomed Opt. 2020;25(4):1–14. https://doi.org/10.1117/1.JBO.25.4.045002
45 Samatham R, Phillips KG, Jacques SL. Assessment of optical clearing agents using reflectance-mode confocal scanning laser microscopy. J Innov Opt Health Sci. 2010;03(03):183–8. https://doi.org/10.1142/s1793545810001064
46 Saletnik Ł, Wesołowski R. Fluorescent spectroscopy of collagen as a diagnostic tool in medicine. J Med Sci. 2022;91(1):584. https://doi.org/10.20883/medical.e584
47 Yuan Y, Liu X, Wang X, Bai T, Du Y, Hao W, et al. Rapid elimination of scattering in three-dimensional fluorescence spectra via deep learning. Spectrochim Acta A. 2025;325:125121. https://doi.org/10.1016/j.saa.2024.125121